ARTICLES
https://doi.org/10.1038/s41563-020-0768-7

nature materials

A natural impact-resistant bicontinuous composite nanoparticle coating

Wei Huang[1,2], Mehdi Shishehbor[3], Nicolás Guarín-Zapata[3], Nathan D. Kirchhofer[4], Jason Li[4], Luz Cruz[5], Taifeng Wang[5], Sanjit Bhowmick[6], Douglas Stauffer[6], Praveena Manimunda[6], Krassimir N. Bozhilov[7], Roy Caldwell[8], Pablo Zavattieri[3] and David Kisailus[1,2,5]✉

Nature utilizes the available resources to construct lightweight, strong and tough materials under constrained environmental conditions. The impact surface of the fast-striking dactyl club from the mantis shrimp is an example of one such composite material; the shrimp has evolved the capability to localize damage and avoid catastrophic failure from high-speed collisions during its feeding activities. Here we report that the dactyl club of mantis shrimps contains an impact-resistant coating composed of densely packed (about 88 per cent by volume) ~65-nm bicontinuous nanoparticles of hydroxyapatite integrated within an organic matrix. These mesocrystalline hydroxyapatite nanoparticles are assembled from small, highly aligned nanocrystals. Under impacts of high strain rates (around $10^4\ s^{-1}$), particles rotate and translate, whereas the nanocrystalline networks fracture at low-angle grain boundaries, form dislocations and undergo amorphization. The interpenetrating organic network provides additional toughening, as well as substantial damping, with a loss coefficient of around 0.02. An unusual combination of stiffness and damping is therefore achieved, outperforming many engineered materials.

There is an urgent need for light-weight, high-performance impact-resistant and energy-absorbent materials in many facets of our society, which include automobile and aerospace engineering[1,2]. Over the past few decades, natural systems have proved an incredible resource for the discovery of new material designs with broad applications[3–6]. This includes implementation towards synthetic impact-resistant materials[4,7,8]. To this end, organisms build these natural composites to ensure their survival against a variety of stresses; this requires clever designs under the constraints of both a limited material selection and a narrow range of synthesis conditions[9,10]. One key consideration in the design of these natural-based constructs is the effect of strain rate[11]. For example, bones in the human body are generally placed under a quasi-static and fatigue loading, whereas deer antlers with similar material components face substantially higher strain-rate impacts ($\sim 10^3\ s^{-1}$) (ref. [12]). Indeed, the antlers are able to endure multiple collisions owing to a lower mineral content and a modified design, which leads to an order-of-magnitude higher energy absorption under impact versus that of human cortical bone[13]. This observation provides insight into the adaptability of structural materials within biological systems to environmental stresses over millions of years of evolution.

One example of a very well studied natural composite is the mollusc shell, which demonstrates a remarkable strength and toughness to resist crush and penetration damage from predators[14,15]. These mollusc shells are a strong and tough biological armour (up to 40 times tougher than its ceramic constituent[10,11]), yet they can still be fractured through high-strain-rate impacts from the strikes of a mantis shrimp, *Odontodactylus scyllarus* (Fig. 1a). Using its dactyl club, a highly developed hammer-like raptorial appendage, this powerful crustacean can generate up to 1,500 N of force by accelerating the club at over ~10,000*g* (a football player can sustain a concussion at 98*g* (ref. [16])) and speeds of $23\ m\ s^{-1}$ (ref. [17]), well beyond the limit that the hard mollusc shell can withstand. At the same time, this feeding behaviour, as well as other daily activities such as ritualized fighting and dwelling construction, necessitates a sufficient amount of energy dissipation within the dactyl club to maintain structural integrity for thousands of future impacts[18]. The multiregional and hierarchical composite structure, as well as the damage mitigation mechanisms of the dactyl club from the smashing type of mantis shrimp, have been studied intensively in recent years[17,19–21]. These studies revealed that a helicoidal arrangement of mineralized alpha-chitin fibres combined with a herringbone architecture, which results from a mineralization gradient, can deflect and twist crack propagation, whereas the striated region, which consists of circumferentially oriented fibres, keeps the club under compression during impact, and thus, as a system, these parts increase the overall toughness of the clubs[19,22]. Although the aforementioned studies provide insights to the mechanisms of toughening in the club, the effects of multiple high-strain-rate impacts, similar to those encountered in the native environment of the mantis shrimp, are still not known, but are of great interest for many engineering applications.

Here we reveal the effects of the high strain rate ($\sim 10^4\ s^{-1}$), microscale impacts of these biological hammers on the hard shells of their prey, specifically an ultrathin (~70-μm) nanoparticle-based coating that protects the underlying fibre-based composite structure from massive contact stresses. Specifically, we uncover the hierarchical nature of these nanoparticles, demonstrate that the impact penetration depth is reduced by at least 50% and reveal multiscale energy dissipation mechanisms that help to mitigate

[1]Department of Chemical and Environmental Engineering, University of California, Riverside, CA, USA. [2]Department of Materials Science and Engineering, University of California, Irvine, CA, USA. [3]Lyles School of Civil Engineering, Purdue University, West Lafayette, IN, USA. [4]Oxford Instruments Asylum Research, Goleta, CA, USA. [5]Materials Science and Engineering Program, University of California, Riverside, CA, USA. [6]Bruker, Minneapolis, MN, USA. [7]Central Facility for Advanced Microscopy and Microanalysis, University of California, Riverside, CA, USA. [8]Department of Integrative Biology, University of California, Berkeley, CA, USA. ✉e-mail: david.k@uci.edu

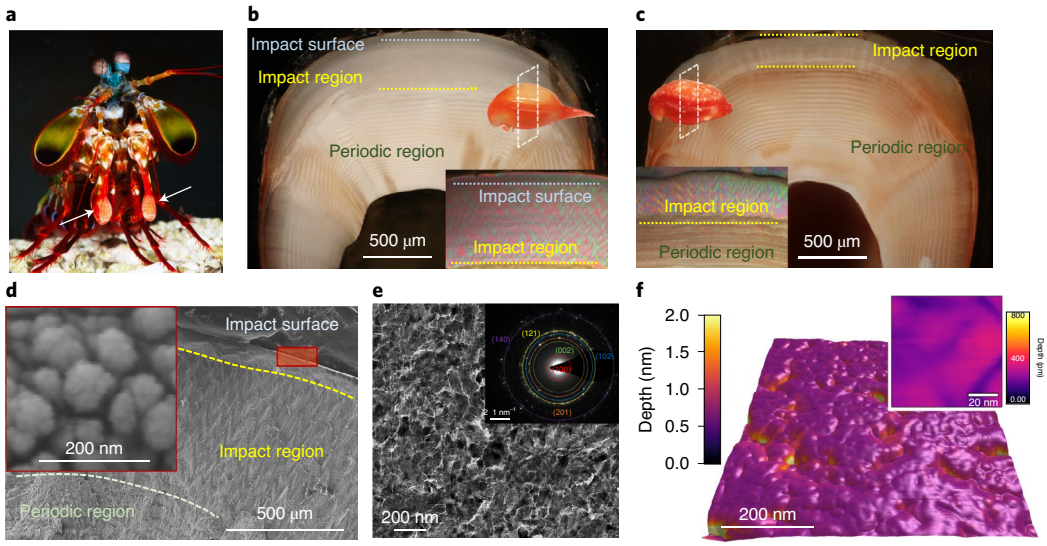

Fig. 1 | Impact surface of the dactyl club of the mantis shrimp. a, Photograph of a mantis shrimp and its dactyl club, indicated with white arrows. **b**,**c**, Optical micrographs of transverse sections of an intact, intermoulted dactyl club (**b**) and a damaged moulted club (**c**). In **b** and **c**, the impact surface, impact region and periodic region are depicted. Insets: differential interference contrast images highlighting the intact (**b**) and worn (**c**) surfaces of the clubs. The damaged moulted clubs and intermoulted clubs in five different mantis shrimps were investigated. Similar features were observed. **d**, SEM micrograph of a transverse section of an intermoulted dactyl club. Inset: nanoparticles ~60 nm in diameter are found within the impact surface. **e**, The TEM micrograph of the nanoparticles confirms the size and volume fraction of the particles in the impact surface (~88%). Inset: the selected area electron diffraction indicates the nanoparticles consist, in part, of HAP. **f**, AFM indentation-depth maps overlaid on 3D topographical maps of the nanoparticles from the red boxed region in **d**. Inset: a higher-resolution AFM indentation map reveals that the ~60-nm particles are composed of smaller grains. Three independent dactyl clubs from three different mantis shrimps were examined with SEM, TEM and AFM. Similar results to those shown in **d**–**f** were observed.

catastrophic failure. Substantial damping (loss coefficient of ~0.02) while maintaining a high stiffness (elastic modulus of ~58.9 GPa) was also observed, a rare combination not common in engineered materials. These findings provide insight towards protecting a broad variety of structures from multiple high-speed impact events that will ultimately prevent catastrophic failure and, more importantly, personal injury.

Nanoparticle-based coating on the surface of a dactyl club

An optical micrograph of a transverse section of the intermoulted (that is, newly formed) dactyl club (Fig. 1b) highlights three independent regions: the outermost ~70-μm-thick coating, which we call the 'impact surface', consists of highly mineralized hydroxyapatite (HAP) nanoparticles; beneath this is the 'impact region', which has a herringbone-like structure of nanocrystalline HAP mineralized chitin fibres; at the core of the club is the 'periodic region', which comprises mineralized (amorphous carbonated calcium phosphate) α-chitin fibres arranged in a helicoidal architecture[19]. Clearly, the intermoulted specimen is completely intact, whereas analysis of the moulted one (that is, heavily used, Fig. 1c) reveals that the outermost impact surface is substantially worn, which suggests loss of the particulate material from high contact stresses during thousands of impacts. Differential interference contrast optical micrographs (Fig. 1b,c insets) highlight the roughened surface of the moulted sample, which further suggests a potential source of energy dissipation in the club, via particle translation and ablation. Additional characterization of a transverse section from a fresh, intermoulted dactyl club via scanning electron microscopy (SEM; Fig. 1d) shows the three distinct regions and highlights the nanoparticulate nature of the impact surface (Fig. 1d inset). These densely packed sub-100-nm nanoparticles, appear as aggregates. Transmission electron microscopy (TEM) of a coronal section of the impact surface validates that the particles (~65.5 ± 15.4 nm) are, indeed, crystalline HAP (Fig. 1e). Quantitative bimodal atomic force microscopy (AFM) imaging of a transverse section was used to obtain a topographical map of this particulate region, which revealed a similar indentation profile among particles (Fig. 1f). A higher-resolution indentation depth map (Fig. 1f inset) shows different nanoscale features within a single particle. Previous work suggests that particles in the impact surface region are single crystalline[19]. However, high-resolution TEM (HRTEM) indicates that these ~65 nm 'single' crystals consist of smaller (~15.9 ± 5.2 nm) primary grains (outlined in yellow in Fig. 2a) that show a preferred orientation within each secondary particle (Extended Data Fig. 1). Comparison of the AFM and TEM images of the impact surface corroborates the average particle size (~65.5 ± 15.4 nm) and the relatively high packing density (~88 vol%). Fast Fourier transform (FFT) analysis of the micrograph in Fig. 2a confirms that the secondary particles are not single crystals, nor randomly oriented polycrystals, but rather highly aligned primary grains, probably formed via an oriented attachment process[23,24]. Higher-resolution imaging (Fig. 2b) of a few primary grains along with FFT analysis of two adjacent grains clearly indicate a slight misalignment of the (100) planes. A high-resolution bright-field image (Fig. 2b inset) of the interface between two grains reveals a low-angle (~1.5°) grain boundary between adjacent primary grains (Fig. 2c).

Closer observation within both secondary and primary particles revealed regions (~3–4 nm) of lower contrast (red arrows in Fig. 2a,b), which suggests the existence of a secondary phase. Phase-contrast maps acquired by AFM (Fig. 2d) further indicate the presence of two different, and probably interpenetrating, materials within this particle system. Specifically, HAP was identified as the mineral phase and a second, organic phase, which probably consists of a hydrated chitin and protein mixture, was revealed[17,25]. Fourier transform infrared spectroscopy of the particles confirmed the presence of this hydrated organic phase, and thermogravimetry

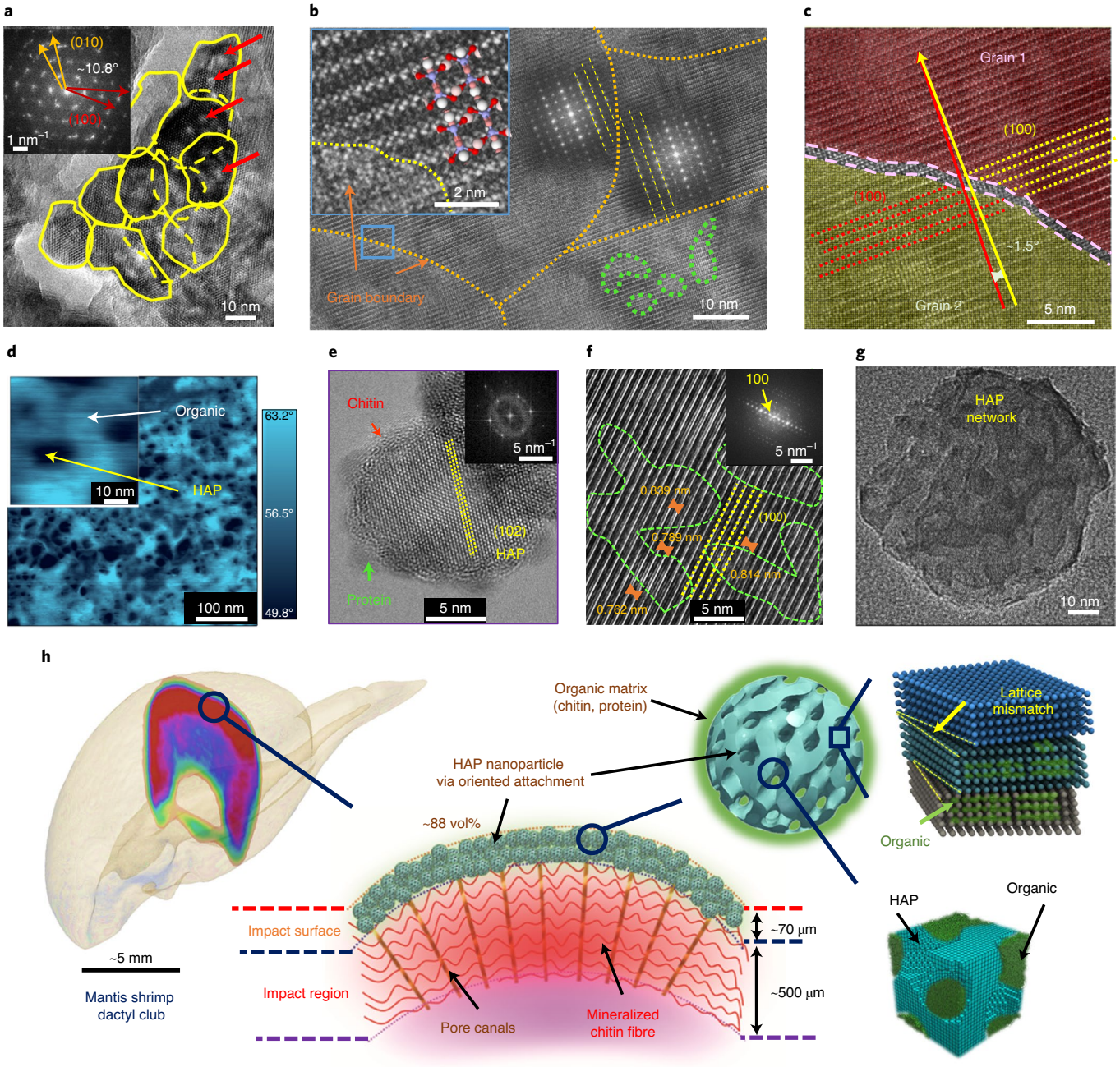

Fig. 2 | Nanoarchitectural design features of particles within the impact surface of the dactyl club. a, Primary grains were found assembled within a single ~60 nm secondary particle. The white dots marked with red arrows suggest a second phase. Inset: the arcs in the FFT pattern indicate the misalignment of primary grains. **b**, Grain boundaries of adjacent grains, indicated by FFT spectroscopy. Inset: HRTEM demonstrating the disordered grain boundary adjacent to the (100) planes of HAP crystals. The second phase found in **a** is outlined in green. **c**, Misalignment (~1.5°) of two adjacent grains. **d**, AFM phase map of a coronal section of the impact surface showing the network of two different phases. The angle (colour scale) refers to the phase change/lag during the AFM tests. The phase change thus reflects changes in mechanical properties. Inset: high-resolution image illustrating the two different phases. **e**, HRTEM of stained samples showing chitin molecules surrounding a HAP crystal lattice. Proteins are stained as dark spots. Inset: FFT pattern of the chitin-wrapped HAP nanoparticles. Diffraction spots represent HAP crystals and the broad diffuse ring represents the chitin macromolecules. **f**, HRTEM image shows the organic network within the HAP crystalline network. The green dashed lines indicate areas that have organic phase, as suggested by the expanded *d* spacings of the lattice. Inset: FFT pattern. **g**, HRTEM of HAP particles after heat treatment at 800 °C. **h**, Schematic of the dactyl club highlighting the impact surface and illustrating its location and hierarchical nature. From left to right: drawing of the dactyl club, with the transverse cutaway highlighted in colour; impact surface and impact region from the transverse section; HAP nanoparticles embedded in an organic matrix on the impact surface; bicontinuous network of the HAP nanoparticles within an organic phase (bottom); oriented attachment of HAP nanocrystals, in which the lattice mismatch and organics embedded within the HAP crystal lattice are illustrated (top). Three independent dactyl clubs from three different mantis shrimps were examined with nanostructures similar to those shown in **a**–**g**.

(TGA) and differential scanning calorimetry (DSC) indicated that the weight fraction of the organic phase was ~17% (Supplementary Fig. 1). Additional TEM analysis revealed chitin molecules adjacent to HAP nanocrystals, and proteins (indicated by high contrast stains in Fig. 2e) appear colocated with the chitin molecules, which suggests their role in assisting the biomineralization process

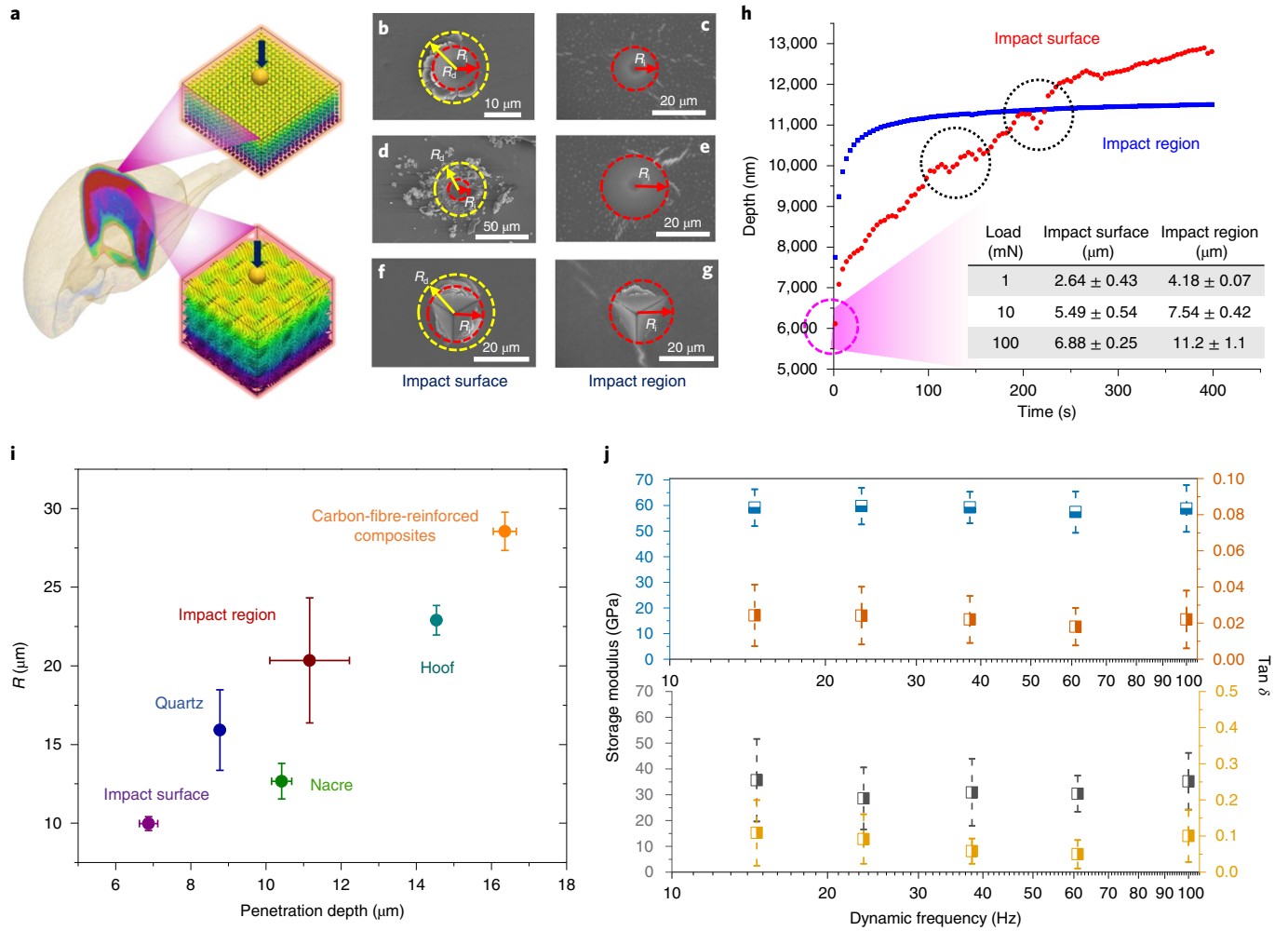

Fig. 3 | Effects of high-strain-rate microimpact tests, damping behaviour and energy dissipation of the impact surface of the dactyl club. a, The schematic highlights the regions interrogated by the impact tests: the impact surface (top) and impact region (bottom) of the dactyl club. **b**–**g**, SEM micrographs of damaged surfaces after microimpacts. **b**,**c**, Impacts from a blunt spherical indenter head on the impact surface (**b**) and the impact region (**c**). **d**,**e**, Surfaces after multiple (that is, 100) impacts on the impact surface (**d**) and the impact region (**e**). **f**,**g**, Impact damage areas from a sharp cube-corner indenter head on the impact surface (**f**) and the impact region (**g**). R_i is the indentation area and R_d is the actual damaged area on the indentation surface. SEM of the damage areas in three independent tests show similar results to those shown in **b**–**g**. **h**, Plots of penetration depth versus the number of impacts during the multiple impact tests. Inset: the table shows the impact depth as a function of impact load on both the impact surface and the impact region for the initial impact. **i**, Relationship of the damage area versus penetration depth of various engineering and biological materials subjected to a high-strain-rate impact. Under the same impact conditions, the impact surface of the dactyl club shows the smallest penetration depth and damage area. $n = 3$ independent locations tested in each material. **j**, Plot of the storage modulus and tan δ as a function of dynamic frequency (acquired from nanoDMA testing) for both the impact surface (top) and the impact region (bottom). $n = 6$ independent locations within the two different biological independent specimens tested. **i**,**j**, Data are presented as mean values ± s.d.

(Fig. 2e and Extended Data Fig. 2)[26,27]. Closer observation of the lighter-contrasted regions in the mineral showed the presence of a strained (100) HAP lattice (Fig. 2f), which indicates the potential effect of occluded organics. Observations of organic networks, incorporated during the biomineralization process, inside inorganic biogenic crystals have been reported previously[28,29]. Here we found that the interpenetrating organic phase can also affect atomic packing within the HAP crystal and induce lattice distortions, as reported in a calcite–protein system[30]. To better understand the distribution of inorganic and organic phases, particles were annealed in air at 800 °C to remove organics. Even after annealing at a high temperature, the particles remained intact, albeit without the organic phase (Supplementary Fig. 2). HRTEM imaging (Fig. 2g) revealed that particles consist of an interpenetrating, bicontinuous network of organic and inorganic phases, which resemble bicontinuous copolymer nanoparticles reported previously[31]. The three-dimensional (3D) bicontinuous network within the particles was further confirmed via a series of TEM images collected at different tilt angles (Supplementary Video 1). Furthermore, by removing the organic phase, the distortion of the (100) lattice disappeared (Supplementary Fig. 2), which validates the existence of the interpenetrating organic network.

The inorganic component, calcium phosphate, has a low solubility under biological synthetic conditions (room temperature and near-neutral pH)[32] and thus reduction of the free energy in this system probably occurs via particle attachment. In many such biomineralization processes, the organic matrix interacts with mineral precursors, which dictate the final morphology and polymorph[28]. In fact, it is likely that the presence of the organic phase (in this case, chitin and proteins) guides the pathway by which nanoparticles

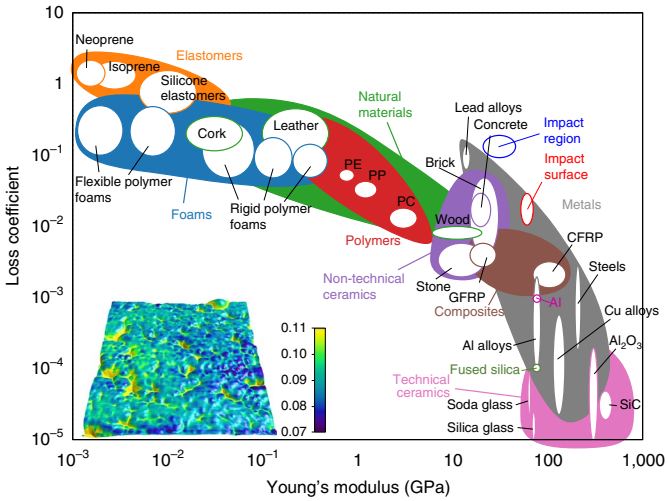

Fig. 4 | Ashby plot of loss coefficient and Young's modulus of synthetic and natural materials. Loss coefficient and Young's modulus data of dactyl clubs acquired from nanoindentation and nanoDMA are incorporated into the plot. GFRP, glass-fibre-reinforced polymer; CFRP, carbon-fibre-reinforced polymer; PE, polyethylene; PP, polypropylene; PC, polycarbonate. Inset: loss coefficient data (colour scale) overlaid on a 3D topographical map of the impact surface acquired from AFM, which highlights the tan δ distribution in HAP and organic phases at the nanoscale. AFM tests on three independent dactyl clubs shows similar results. Figure adapted with permission from ref. [41], Elsevier.

aggregate[33–35], seemingly in a highly controlled manner (that is, oriented attachment), which enables near-perfect alignment of neighbouring crystalline domains (Fig. 2h)[17,24]. The subsequent interfaces between primary grains are low-angle grain boundaries (~1.5°). These low-angle grain boundaries not only reduce the free energy of formation for this inorganic network, but can also potentially provide substantial toughening during impact via their ability to be fractured at these interfaces, analogous to tempered glass shattering into small pieces and dissipating large amounts of energy[36]. In addition, the organic phases that influence the mineralization process can also be occluded within the inorganic crystal, which provides a substantially higher fracture toughness, hardness, energy dissipation and damping behaviour[30,37,38]. The addition of this impact surface, therefore, probably acts as a protective layer for the underlying impact region (as illustrated in Fig. 2h), and is discussed in the following sections.

High strain-rate microimpacts and damping behaviour

To understand the response of the composite particle-based coating of the impact surface during the high-strain-rate-impact feeding activities of the mantis shrimp, microimpact tests (strain rate ~10^4 s^{-1}) were conducted on dactyl club samples (Fig. 3a), with and without the protection of this particulate coating (that is, directly on the impact surface or on the impact region, respectively). Both spherical and cube corner indenter heads were used in these tests to mimic the conditions of blunt or sharp contacts the dactyl club might encounter. The damage fields of the impact surface (Fig. 3b,d,f) and impact region (Fig. 3c,e,g) were examined after (1) a single spherical (blunt) impact (Fig. 3b,c), (2) 100 sequential spherical (blunt) impacts (Fig. 3d,e) and (3) a single cube-corner (sharp) impact (Fig. 3f,g). Particle pile-up was observed in the impact surface (Fig. 3b), with cracks identified in the impact region (Fig. 3c). A similar scenario occurred in both samples after 100 impacts with the spherical indenter, but particles were worn off the impact surface (Fig. 3d), whereas more extensive cracks propagated in the impact region (Fig. 3e). Different deformation mechanisms were found in samples impacted with a sharp cube-corner indenter head (Fig. 3f,g). Even at different loads (1, 10 and 100 mN), the observed penetration depth of the samples with the impact surface present (the native dactyl club) was only one-half that measured in the samples without it (that is, directly on the impact region) (Fig. 3h). Additional strikes to the impact surface resulted in a gradual increase in the penetration depth, which included depth fluctuations (black dashed circles in Fig. 3h) probably due to the rotation and translation of the composite nanoparticles. Conversely, the depth of penetration on the impact region increased for the first few impacts, but reached a plateau with additional strikes. This can be explained by the different deformation mechanisms in the impact surface and impact region under these high-strain-rate microimpacts. The impact surface is able to localize damage and prevent crack initiation and propagation during multiple impacts, whereas more cracks are initiated and propagated in the impact region (that is, without the presence of a protective nanoparticle coating). The calculated energy absorption density (that is, energy absorption per volume) of the impact surface is ~0.237 nJ μm^{-3}, which is nearly twice the value in nacre (~0.128 nJ μm^{-3}) under similar high-strain-rate impacts. Figure 3i provides a comparison of penetration resistance and damage areas under high-strain-rate impacts in various biological and engineering structural materials. The impact surface has the smallest damage area and penetration depth, which indicates the exceptional energy dissipation efficiency of the dactyl club under high-strain-rate conditions. These findings agree with our hypothesis that the particulate layer on the impact surface has a substantial role in preventing catastrophic failure of the club during thousands of high-strain-rate impacts. By comparing the damage modes under quasi-static indentation and high-strain-rate impacts, we note that the damage is more localized under the high-strain-rate impact, whereas more cracks initiate and propagate between the larger, secondary nanoparticles in the samples subjected to quasi-static indentation (Extended Data Fig. 3). Here, it is likely that under a high-strain-rate impact, chitin and proteins within and between the nanoparticles stiffen, which leads to the localized failure of the particles and so cracking between the particles is thus limited[39,40]. This strain-rate-dependent behaviour suggests that the ultrathin biological coating found in the mantis shrimp dactyl club is designed to avoid catastrophic damage during high-strain-rate impacts and ensure efficient feeding and thus survival.

In addition to localizing the damage area and preventing crack propagation, the particulate layer has promising damping effects to accommodate both a high acceleration and velocity impacts. The loss coefficient and storage modulus of the impact surface and impact region were measured using AFM and a nanoindenter equipped with nanoscale dynamic mechanical analysis (nanoDMA III) (Supplementary Figs. 3 and 4). The storage modulus of the impact surface was 58.9 ± 8 GPa, with a loss coefficient of 0.02 ± 0.01, whereas the impact region had a modulus 32.6 ± 12 GPa, and a higher loss coefficient of 0.1 ± 0.07 (Fig. 3j). The Ashby plot of stiffness and loss coefficient in biological and engineering materials shows that the loss tangent (tan δ) value of both the impact region and the impact surface are larger than those of most metals and composites with similar stiffnesses (Fig. 4)[41]. In the impact surface, this might be attributed to the bicontinuous nature of the nanoparticles. As a result, the deceleration in the impact surface occurs faster than that in aluminium and fused silica, which indicates better damping properties without sacrificing the stiffness (Supplementary Fig. 5). Carbon-fibre-reinforced polymers that could be used for automobiles and aircraft have a similar stiffness to that of the impact surface coatings (~70–100 GPa), yet are an order of magnitude lower in loss coefficient, which suggests the implementation of the design elements from these coatings could yield improvements in noise and vibration damping[42,43].

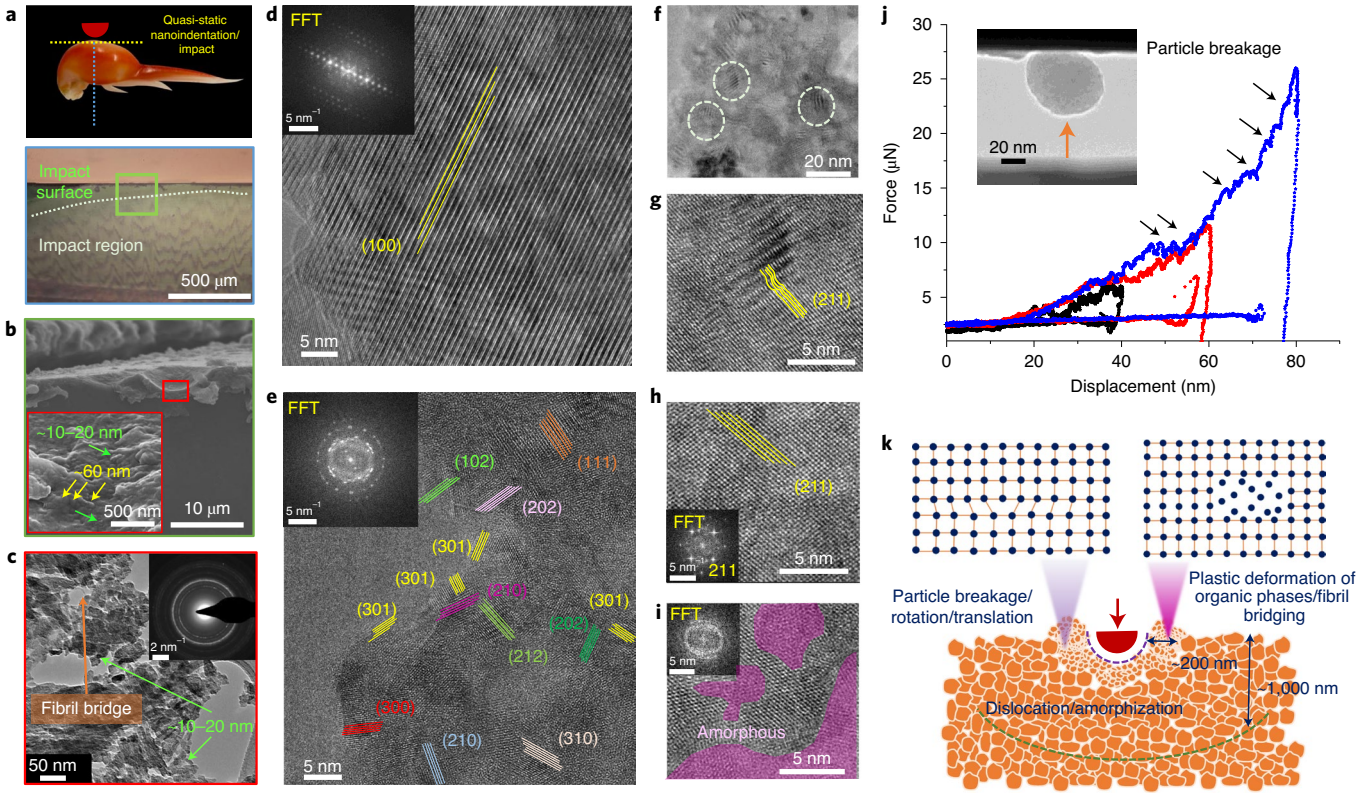

Fig. 5 | Nanoscale energy dissipation mechanisms of the impact surface of the dactyl club. a, Region of contact (coronal plane) for the quasi-static indentation and microimpact tests. The optical micrograph (bottom) highlights the damaged areas. **b**, SEM micrograph of the transverse section of the damaged area after a high-strain-rate impact. Inset: the surface of the impact indicates both large (~60 nm) and small (~10–20 nm) nanoparticles. **c**, TEM micrograph of the damaged area (red box in **b**) confirms the presence of ~10–20 nm nanoparticles. Analysis of the selected area electron diffraction pattern reveals randomly oriented nanocrystals, formed from the fracture of mesocrystalline particles in the high-strain-rate impact (Fig. 1f). **d**,**e**, HRTEM micrograph illustrating the modification of the ordered grains before the impact (**d**) and after the rotation and translation under the high-strain-rate impact (**e**). **f**, Dislocations (ringed by dashed circles) induced by impact. **g**, Higher magnification of dislocations (yellow lines) within (211) planes. **h**,**i**, Comparison between perfect (**h**) and impact-induced amorphization (**i**) in (211) planes. The observations shown in **a**–**i** were made in three independent dactyl club samples after impact tests. **j**, Load versus displacement curves of in situ TEM compression of a single nanoparticle. Black, red and blue curves show three continuous loading cycles of a single particle. Particle fracture is indicated with black arrows. **k**, Schematic and summary of the nanoscale toughening mechanisms of impact surface composite nanoparticles from high-strain-rate impacts.

Nanoscale energy dissipation mechanisms

The potential mechanisms of energy dissipation and damping behaviour within the nanoparticle-based coatings were evaluated by examining the region of impacts (highlighted by the green box in Fig. 5a). Although quasi-static indentation incurred no changes of HAP particle size and shape (Extended Data Fig. 3i,j), high-strain-rate impacts (~$10^4\,s^{-1}$) led to a substantial fracture of secondary HAP particles into smaller (~10–20 nm) primary grains (Fig. 5b,c as well as Supplementary Fig. 6) and thus dissipated some of the impact energy. Particle breakage can also be validated via a comparison of the selected area electron diffraction patterns from specimens before and after impact, in which intact samples consisted of a mesocrystalline structure (Extended Data Fig. 1a,b), whereas impacted samples were pulverized and consisted of randomized grains (Fig. 5c inset). Analysis of the grains in impacted samples via HRTEM revealed fractured secondary particles with a subsequent randomization of the orientations of the resultant primary grains (Fig. 5d,e). In addition, the high-strain-rate impacts induced crystal imperfections in HAP crystals: dislocations (via nucleation, glide and annihilation) and regions of amorphization (Fig. 5f–i), which have also been observed in nacre after high-strain-rate impacts[44]. We highlight these changes as additional sources of energy dissipation. High strain-rate or shock-induced dislocation formation as well as amorphization were reported in synthetic and natural ceramics, and were considered as efficient energy-dissipation mechanisms[44,45].

To quantify the amount of energy absorption by breaking the secondary particles, in situ TEM compression tests on single HAP nanoparticles, separated from the club, were performed. The load–displacement curves are shown in Fig. 5j, in which different loading cycles are marked in different colours. The plateaus on the curves indicate cracking events and particle breakage[20], which lead to a total energy dissipation of 6.23×10^{-4} nJ until particle failure (Extended Data Fig. 4). The energy dissipation density is ~4.55 nJ μm^{-3}, which is an order of magnitude higher than a previously reported bioceramic armour (~0.29 nJ μm^{-3}) (ref. [14]). The nanoparticle is able to recover to its original shape after ~80% compression (Supplementary Video 2). This large deformation, as well as the ability to recover, is attributed to the bicontinuous nature of the hydrated organic networks[46]. A schematic shown in Fig. 5k highlights the energy absorption mechanisms of these nanoparticle coatings under a high-strain-rate impact. The total energy calculated from the area under the stress–strain curves is the contribution of plastic deformation from the organic network as elastic energy is released by crack initiation and propagation in the HAP mesocrystalline network. In addition, by implementing the bicontinuous design into the nanoparticle structures, the stiffness and strength are substantially increased

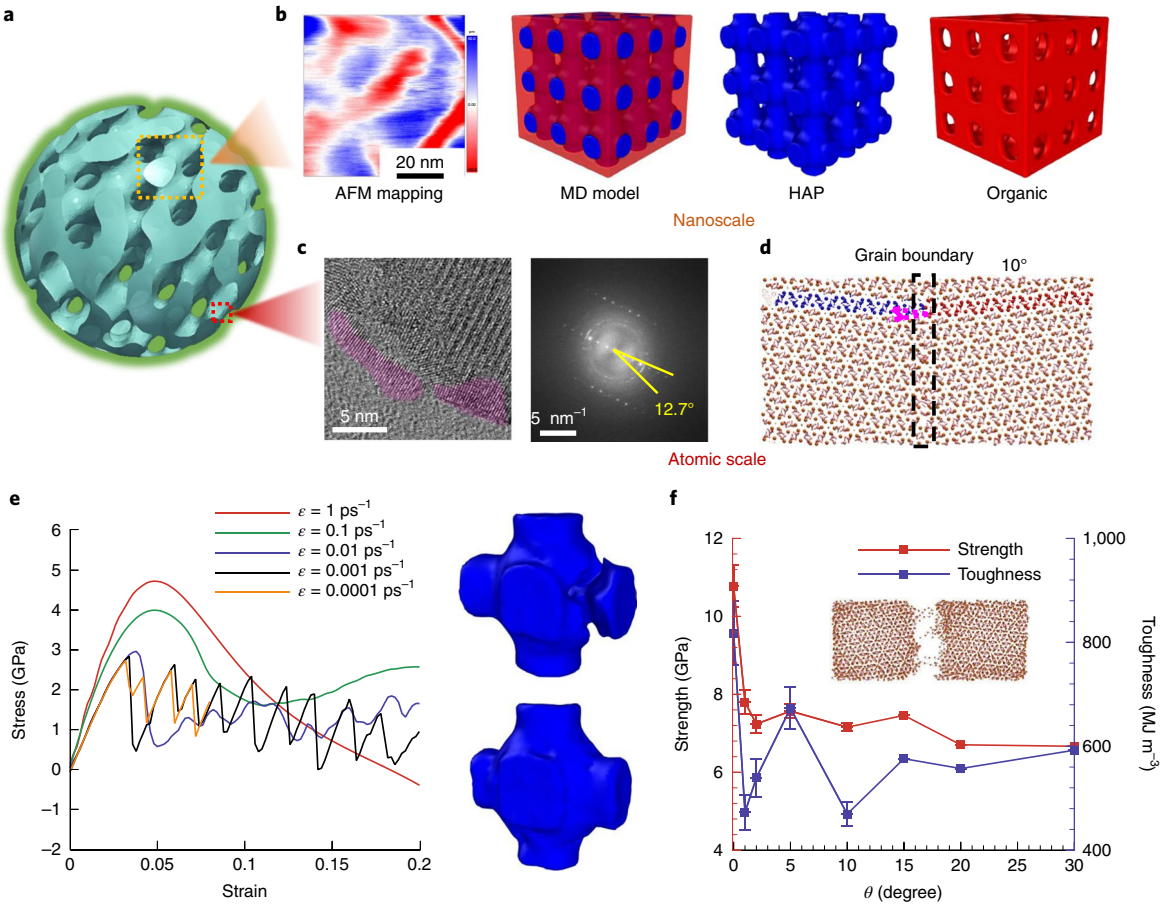

Fig. 6 | Molecular dynamic simulations of the energy dissipation in the bicontinuous HAP nanoparticles. a Schematic of the bicontinuous nanoparticles. **b**, AFM mapping and MD models of the bicontinuous structure at the nanoscale. Blue and red colours indicate HAP and the organic phase, respectively. AFM mapping on three independent dactyl clubs shows similar results. **c**, Left: HRTEM of regions of highly oriented, mesocrystalline particles at the edge of the HAP network are shaded in pink. Right: FFT pattern of a single particle from the HRTEM image. The arc marked with yellow lines shows the misalignment of the primary particles shown in the pink region (left). The angle that the arc covers is ~12.7°. Similar mesocrytalline structures and misalignments were observed in three independent dactyl clubs. **d**, MD model showing the grain boundary between two adjacent HAP single crystals. **e**, MD simulation results of the stress–strain curves of the bicontinuous models, which show a strain-rate dependent behaviour. Localized breakage of the HAP phase occurs at a low strain-rate compression (top, right), whereas uniformly distributed strain is observed at high-strain-rate impacts (bottom, right). **f**, Strength and toughness as a function of grain-boundary angle. Data were acquired from three different initial configurations after equilibrium, and are presented as mean values ± s.d.

compared with those of structures with non-integrated phases, such as traditional composites, which leads to a higher energy absorption[47]. The advantages in energy absorption of bicontinuous phases have been demonstrated in other materials, which include a carbon/epoxy system[48]. However, these ceramic/polymer bicontinuous nanostructures occur in biological materials, specifically in structures that undergo high-strain-rate impacts, which suggests promising energy absorption capabilities. Researchers have applied block copolymer and sol–gel methods to realize synthetic pathways to bicontinuous nanostructures[31,49]. Recently, the 3D printing of resins that phase separate was successfully used to fabricate large-volume samples with bicontinuous nanostructures[50].

To validate our hypotheses regarding the multiple mechanisms of energy dissipation, molecular dynamics (MD) simulations were performed to evaluate the mechanical behaviour at two length scales: at the nanoscale, the strain-rate-dependent behaviour of the bicontinuous network was studied; at the atomic scale, the relation between the angle of the misalignment in the oriented attached particles and the amount of energy dissipated by breakage of the low-angle grain boundaries during the high-strain-rate-impact events was investigated (Fig. 6). MD models of the HAP crystals with different grain-boundary angles were created to simulate the mesocrystalline structure of the impact surface (Fig. 6d). Simulations of the fracture of the bicontinuous particle suggest that the stiffness and strength of the nanoparticles increase as the strain rate increases (Fig. 6e). The deformation of the HAP is more uniform at a higher strain rate, but more localized at a lower strain rate. These correspond to the experimental results that under high strain rate impacts, the uniform stress distribution and lack of plasticity leads to the fracture of the bicontinuous particles (Fig. 5d,e). We note that by having small grain boundaries, the overall strength of the HAP crystals decreases, but enables fractures to occur at these grain boundaries under a high-strain-rate impact (Fig. 6f). The energy dissipation density of the grain boundary fracture is ~0.6 nJ μm^{-3}, which is slightly higher than the overall impact energy absorption density in the experiments (0.237 nJ μm^{-3}). This indicates that the breakage of particles can be the main energy dissipation mechanism under a high-strain-rate impact. In addition, the amorphization work calculated via MD simulation is ~0.038 nJ μm^{-3}, which accounts for ~16% of the overall impact energy (Supplementary Fig. 7).

Outlook

This study provides experimental observation as well as computational validation of the effects of high-strain-rate microscale impacts on biological composites, specifically the ultrathin (~70-μm) nanoparticulate coatings of a dactyl club. These observations suggest the bottom-up controlled synthesis of these materials, which is constrained by biological synthetic parameters (that is, room temperature and limited solubility), can still lead to well engineered structures via highly orchestrated (that is, kinetically controlled) growth. Utilization of these mesocrystalline materials, formed via the oriented attachment around organic networks, not only can reduce the energy of formation of these particles, but can also lead to a lower barrier to fracture, which can enable large and localized energy absorption. By combining the current synthesis and advanced manufacturing methods with design elements from these biological structures, potential blueprints for a new generation of advanced materials with a broad range of application, which includes impact- and vibration-resistant coatings for buildings, body armour, aircraft and automobiles, as well as in abrasion- and impact-resistant wind turbines, can be realized.

Online content

Any methods, additional references, Nature Research reporting summaries, source data, extended data, supplementary information, acknowledgements, peer review information; details of author contributions and competing interests; and statements of data and code availability are available at https://doi.org/10.1038/s41563-020-0768-7.

Received: 30 November 2019; Accepted: 14 July 2020;
Published online: 17 August 2020

References

1. Bhatnagar, A. *Lightweight Ballistic Composites: Military and Law-Enforcement Applications* (Woodhead, 2016).
2. Dalili, N., Edrisy, A. & Carriveau, R. A review of surface engineering issues critical to wind turbine performance. *Renew. Sustain. Energy Rev.* **13**, 428–438 (2009).
3. Munch, E. et al. Tough, bio-inspired hybrid materials. *Science* **322**, 1516–1520 (2008).
4. Grunenfelder, L. et al. Bio-inspired impact-resistant composites. *Acta Biomater* **10**, 3997–4008 (2014).
5. Yaraghi, N. A. & Kisailus, D. Biomimetic structural materials: inspiration from design and assembly. *Annu Rev. Phys. Chem.* **69**, 23–57 (2018).
6. Chen, P. Y., McKittrick, J. & Meyers, M. A. Biological materials: functional adaptations and bioinspired designs. *Prog. Mater. Sci.* **57**, 1492–1704 (2012).
7. Yin, Z., Hannard, F. & Barthelat, F. Impact-resistant nacre-like transparent materials. *Science* **364**, 1260–1263 (2019).
8. Gu, G. X., Takaffoli, M. & Buehler, M. J. Hierarchically enhanced impact resistance of bioinspired composites. *Adv. Mater.* **29**, 1700060 (2017).
9. Huang, W., Zaheri, A., Jung, J.-Y., Espinosa, H. D. & Mckittrick, J. Hierarchical structure and compressive deformation mechanisms of bighorn sheep (*Ovis canadensis*) horn. *Acta Biomater.* **64**, 1–14 (2017).
10. Wegst, U. G. K., Bai, H., Saiz, E., Tomsia, A. P. & Ritchie, R. O. Bioinspired structural materials. *Nat. Mater.* **14**, 23–36 (2015).
11. Huang, W. et al. Multiscale toughening mechanisms in biological materials and bioinspired designs. *Adv. Mater.* **31**, 1901561 (2019).
12. Schaffler, M., Radin, E. & Burr, D. Mechanical and morphological effects of strain rate on fatigue of compact bone. *Bone* **10**, 207–214 (1989).
13. Launey, M. E., Chen, P.-Y., McKittrick, J. & Ritchie, R. Mechanistic aspects of the fracture toughness of elk antler bone. *Acta Biomater.* **6**, 1505–1514 (2010).
14. Li, L. & Ortiz, C. Pervasive nanoscale deformation twinning as a catalyst for efficient energy dissipation in a bioceramic armour. *Nat. Mater.* **13**, 501–507 (2014).
15. Shin, Y. A. et al. Nanotwin-governed toughening mechanism in hierarchically structured biological materials. *Nat. Commun.* **7**, 10772 (2016).
16. Pellman, E. J., Viano, D. C., Tucker, A. M., Casson, I. R. & Waeckerle, J. F. Concussion in professional football: reconstruction of game impacts and injuries. *Neurosurgery* **53**, 799–814 (2003).
17. Weaver, J. C. et al. The stomatopod dactyl club: a formidable damage-tolerant biological hammer. *Science* **336**, 1275–1280 (2012).
18. Caldwell, R. L. & Dingle, H. Stomatopods. *Sci. Am.* **234**, 80–89 (1976).
19. Yaraghi, N. A. et al. A sinusoidally architected helicoidal biocomposite. *Adv. Mater.* **28**, 6835–6844 (2016).
20. Amini, S., Tadayon, M., Idapalapati, S. & Miserez, A. The role of quasi-plasticity in the extreme contact damage tolerance of the stomatopod dactyl club. *Nat. Mater.* **14**, 943–950 (2015).
21. Grunenfelder, L. K. et al. Ecologically driven ultrastructural and hydrodynamic designs in stomatopod cuticles. *Adv. Mater.* **30**, 1705295 (2018).
22. Suksangpanya, N., Yaraghi, N. A., Kisailus, D. & Zavattieri, P. Twisting cracks in Bouligand structures. *J. Mech. Behav. Biomed.* **76**, 38–57 (2017).
23. Cölfen, H. & Mann, S. Higher-order organization by mesoscale self-assembly and transformation of hybrid nanostructures. *Angew. Chem. Int. Ed.* **42**, 2350–2365 (2003).
24. De Yoreo, J. J. et al. Crystallization by particle attachment in synthetic, biogenic, and geologic environments. *Science* **349**, aaa6760 (2015).
25. Rinaudo, M. Chitin and chitosan: properties and applications. *Prog. Polym. Sci.* **31**, 603–632 (2006).
26. Neville, A. & Luke, B. A two-system model for chitin–protein complexes in insect cuticles. *Tissue Cell* **1**, 689–707 (1969).
27. Watson, M. L. Staining of tissue sections for electron microscopy with heavy metals. *J. Cell Biol.* **4**, 475–478 (1958).
28. Gordon, L. M. & Joester, D. Nanoscale chemical tomography of buried organic–inorganic interfaces in the chiton tooth. *Nature* **469**, 194–197 (2011).
29. Li, H., Xin, H. L., Muller, D. A. & Estroff, L. A. Visualizing the 3D internal structure of calcite single crystals grown in agarose hydrogels. *Science* **326**, 1244–1247 (2009).
30. Kim, Y.-Y. et al. Tuning hardness in calcite by incorporation of amino acids. *Nat. Mater.* **15**, 903 (2016).
31. McKenzie, B. E. et al. Controlling internal pore sizes in bicontinuous polymeric nanospheres. *Angew. Chem. Int. Ed.* **54**, 2457–2461 (2015).
32. Zhang, Q., Liu, S.-J. & Yu, S.-H. Recent advances in oriented attachment growth and synthesis of functional materials: concept, evidence, mechanism, and future. *J. Mater. Chem.* **19**, 191–207 (2009).
33. Cöelfen, H. & Antonietti, M. *Mesocrystals and Nonclassical Crystallization* (John Wiley & Sons, 2008).
34. Nudelman, F. et al. The role of collagen in bone apatite formation in the presence of hydroxyapatite nucleation inhibitors. *Nat. Mater.* **9**, 1004–1009 (2010).
35. Song, R. Q. & Cölfen, H. Mesocrystals—ordered nanoparticle superstructures. *Adv. Mater.* **22**, 1301–1330 (2010).
36. Nielsen, J. H. Remaining stress-state and strain-energy in tempered glass fragments. *Glass Struct. Eng.* **2**, 45–56 (2017).
37. Cho, K. R. et al. Direct observation of mineral–organic composite formation reveals occlusion mechanism. *Nat. Commun.* **7**, 10187 (2016).
38. Kim, Y.-Y. et al. An artificial biomineral formed by incorporation of copolymer micelles in calcite crystals. *Nat. Mater.* **10**, 890–896 (2011).
39. Sato, M., Schwarz, W. H. & Pollard, T. D. Dependence of the mechanical properties of actin/α-actinin gels on deformation rate. *Nature* **325**, 828–830 (1987).
40. Jin, K., Feng, X. & Xu, Z. Mechanical properties of chitin–protein interfaces: a molecular dynamics study. *BioNanoScience* **3**, 312–320 (2013).
41. Ashby, M. F. *Materials Selection in Mechanical Design* (Butterworth-Heinemann, 2011).
42. Unwin, A. P. et al. Escaping the Ashby limit for mechanical damping/stiffness trade-off using a constrained high internal friction interfacial layer. *Sci. Rep.* **8**, 2454 (2018).
43. Chung, D. Materials for vibration damping. *J. Mater. Sci.* **36**, 5733–5737 (2001).
44. Huang, Z. W. et al. Uncovering high-strain rate protection mechanism in nacre. *Sci. Rep.* **1**, 148 (2011).
45. Chen, M., McCauley, J. W. & Hemker, K. J. Shock-induced localized amorphization in boron carbide. *Science* **299**, 1563–1566 (2003).
46. Huang, W. et al. How water can affect keratin: hydration-driven recovery of bighorn sheep (*Ovis canadensis*) horns. *Adv. Funct. Mater.* **29**, 1901077 (2019).
47. Cho, H. et al. Engineering the mechanics of heterogeneous soft crystals. *Adv. Funct. Mater.* **26**, 6938–6949 (2016).
48. Lee, J.-H., Wang, L., Boyce, M. C. & Thomas, E. L. Periodic bicontinuous composites for high specific energy absorption. *Nano Lett.* **12**, 4392–4396 (2012).
49. Gutierrez, J., Tercjak, A. & Mondragon, I. Conductive behavior of high TiO_2 nanoparticle content of inorganic/organic nanostructured composites. *J. Am. Chem. Soc.* **132**, 873–878 (2010).
50. Moore, D. G., Barbera, L., Masania, K. & Studart, A. R. Three-dimensional printing of multicomponent glasses using phase-separating resins. *Nat. Mater.* **19**, 212–217 (2020).

Methods

Sample preparation. Live specimens of *O. scyllarus* were obtained from a commercial supplier and maintained in a lab seawater system. The moulting cycles of the specimens were monitored and recorded. Fresh and intact dactyl clubs were collected one week after moulting. Heavily damaged clubs were collected from the moulted specimens. Optical micrographs (Zeiss) were obtained of both intact and damaged samples via polished cross-sections. Samples were first embedded in epoxy (System 2000, Fibreglast) and then polished with progressively finer silicon carbide and diamond abrasives down to 50-nm grit. Fractured samples for SEM imaging were acquired using a sharpened chisel. An ultramicrotome (RMC MT-X, Boeckeler Instruments) was utilized to polish sample surfaces, which were further characterized with nanoindentation, microimpact testing and AFM.

Electron microscopy. Fractured surfaces, microtomed sections and damaged surfaces of dactyl clubs via quasi-static indentation or high-strain-rate microimpacts were examined using SEM (TESCAN MIRA3 GMU). Samples were mounted to aluminium pin mounts and coated with platinum and palladium for 60 s before imaging.

For transmission microscopy imaging, intact fresh dactyl-club specimens were first fixed using glutaraldehyde (2.5%) aqueous sodium phosphate buffer solution (0.1 M, pH = 7.2) for 2 h and then washed in deionized water three times for 5 min each. Samples were then serially dehydrated in ethanol and embedded in resin (Epofix Cold-Setting Embedding Resin, Electron Microscopy Sciences) in silicon moulds at room temperature overnight. Thin sections (~70 nm) were then acquired by using an ultramicrotome (RMC MT-X, Boeckeler Instruments) and a diamond knife (PELCO, Ted Pella). The thin sections were then placed on carbon-coated copper grids for further imaging. Another set of grids with microtomed thin sections were stained with 1% uranyl acetate solution for 10 min, followed by rinsing with deionized water three times and drying with filter paper. The samples were further stained with 0.1% lead citrate for 60 s within a CO_2-free environment by putting NaOH pellets in the staining chamber. TEM and HRTEM images were taken by a FEI Tecnai12 at 120 kV and a FEI Titan Themis 300 at 300 kV (Thermo Fisher Scientific), respectively.

Schematics of the nanostructures observed in HRTEM were further generated with Solidworks 2019 and Vesta 3.4.5.

AFM. Coronal and transverse surfaces were polished via an ultramicrotome. Quantitative bimodal AFM imaging was performed on both surfaces using a commercially available Cypher ES AFM (Oxford Instruments Asylum Research). This technique allowed for the simultaneous tracking of topography, phase and amplitude using amplitude modulation of the first oscillatory eigenmode of the cantilever, whereas frequency shift and energy dissipation were tracked with frequency modulation of the second eigenmode at a much smaller amplitude. Together, these enabled the calculations of indentation depth, storage modulus and tan δ of a sample as previously reported[51–53]. Briefly, for tan δ, the cantilever resonance frequency and stiffness were calibrated with the GetReal software protocol, whereas the optical lever sensitivity and absolute phase, ϕ_{free}, were set by fitting a thermal resonance spectrum. After choosing the resonant frequency amplitude, A_{free}, for the free (non-surface-interacting) cantilever, the tip–sample interaction amplitude, A_{int}, and phase, ϕ_{int}, were collected at every pixel (that is, during imaging) and used to calculate tan δ via the equation $\tan\delta = \frac{A_{free}\sin\phi_{int} - A_{int}\sin\phi_{free}}{A_{free}\cos\phi_{int} - A_{int}\cos\phi_{free}}$ in real time. An Olympus AC160TSA-R3 cantilever was used (Au reflex coating), and driven with blueDrive photothermal excitation. The nominal spring constant, first eigenmode resonance and tip radius of this lever are $k = 26\,\mathrm{N\,m^{-1}}$, $f = 300\,\mathrm{kHz}$ and $R = 7\,\mathrm{nm}$, respectively. The experimentally measured values for this cantilever's first eigenmode were $k_1 = 34.5\,\mathrm{N\,m^{-1}}$, $f_1 = 259.3\,\mathrm{kHz}$ and $R_{tip} = 7.7\,\mathrm{nm}$. The measured values for the second eigenmode were $k_2 = 613.4\,\mathrm{N\,m^{-1}}$ and $f_2 = 1.455\,\mathrm{MHz}$.

Nanoindentation and nanoDMA. Nanoindentations on both transverse and coronal polished surfaces of the dactyl clubs were performed using a Hysitron TI-980 TriboIndenter (Bruker Nano Surfaces) utilizing nanoDMA III. To measure the composite response of the impact surface coating, a 1-μm-diamond-conospherical probe was selected for testing. Frequency sweep tests were conducted at different locations on the impact surface and impact region at a fixed normal load (1.5 mN) using the reference frequency technique[54,55]. The probe oscillation frequency was varied logarithmically from to 100 Hz. Storage (E'), loss modulus (E'') and tan δ were calculated using the equations:

$$E' = \frac{k_s\sqrt{\pi}}{2\sqrt{A_c}},\quad E'' = \frac{\omega C_s\sqrt{\pi}}{2\sqrt{A_c}},\quad \tan\delta = \frac{E''}{E'} \qquad (1)$$

where k_s is the storage stiffness, C_s the loss stiffness, ω the frequency and A_c a contact area. The tip area function was generated via fused quartz testing in the usual fashion.

TGA and DSC. HAP nanoparticles were acquired from the impact surface of six clubs. The HAP powders were then tested with TGA and DSC performed on a TGA/DSC 3+ Mettler Toledo under flowing air from 25 to 800 °C at a heating rate of 10 °C min^{-1}. The postannealed particles were further characterized with SEM and TEM.

Quasi-static indentation and high-strain-rate microimpact tests. Flat coronal surfaces were prepared by an ultramicrotome, and were further used in quasi-static nanoindentation and microimpact tests. A TI 950 TriboIndenter (Bruker) was used to perform the quasi-static nanoindentation tests. Cube-corner and spherical (tip radius 5 μm) diamond indenter heads were used during the tests. Specimens were loaded to 100, 300 and 500 mN. High strain-rate microimpact tests were conducted on the NanoTest Vantage (Micro Materials). The impact heads were either cube corner or spherical (tip radius 5 μm) diamond indenter heads, which were the same as those used in the quasi-static nanoindentation tests. An acceleration distance of 10 μm reached the highest strain rate of ~$10^4\,\mathrm{s^{-1}}$. The impact load was set at 100 mN. Both the impact surface and the impact region of the dactyl club specimens were tested in quasi-static indentation and under microimpact. The damaged areas after indentations and impacts were subsequently imaged by SEM and HRTEM. Nacre, equine hoof, quartz and carbon-fibre-reinforced composites were purchased from commercial sources. Samples were embedded in epoxy and polished for further microimpact tests. The impact testing conditions were the same as those for the tests performed on the impact surface and impact region. The damaged areas were further imaged using optical microscopy and SEM. The total impact energy can be calculated as $E = \frac{1}{2}mv^2$, where m is the mass of the indenter head and v is the impact velocity. The total volume of deformation can be estimated from $V = \pi d R_d^2/3$, in which R_d is the radius of the damage area and d is the penetration depth. Thus, the energy absorption density (energy absorption per volume) can be calculated as E/V. Mechanical test data were processed with Origin 9.0.

In situ TEM compression tests. HAP nanoparticles were acquired by first scratching a fresh dactyl club surface with a razor blade to obtain the HAP powders. The powders were then dispersed in deionized water and sonicated for 4 h. The suspension was subsequently centrifuged for 5 min at 3,000 r.p.m. The size of the HAP nanoparticles was confirmed by SEM and dynamic light scattering (Zetasizer Ultra, Malvern Panalytical Ltd). The supernatant was then dropped onto a 1 μm silicon wedge for further in situ TEM compression tests. A Hysitron PI 95 TEM PicoIndenter (Bruker) was used to perform the compression tests in a Tecnai12 TEM (Thermo Fisher Scientific) at 120 kV. A flat punch indenter head with a tip diameter of 1 μm was used in the compression test. The loading rate was $1\,\mathrm{nm\,s^{-1}}$.

MD modelling. To understand the effect of grain boundary on the strength and toughness of HAP, MD simulations were performed using the LAMMPS package[56] and by employing the INTERFACE-CVFF forcefield previously developed for the structure and elastic modulus of HAP and the results are in good agreement with the experimental data[57]. In addition, the strength of HAP from our simulations is in agreement with those reported values from ab initio calculations[58]. In this study, the monoclinic structure of HAP with space group $P21/b$ and unit cell parameters of 9.421 Å × 18.843 Å × 6.881 Å with $\alpha = 90°$, $\beta = 90°$ and $\gamma = 120°$, according to the experimental observations, was used[59]. To study the grain boundary effect, eight models of HAP bicrystals, that represented different misorientation angles of $\theta = 0$, 1, 2, 5, 10, 15, 20 and 30° were generated (as shown in Fig. 6d for $\theta = 10°$). For each model, the HAP unit cell was initially replicated by 9 × 5 × 4 to obtain a large super cell with dimensions of 84 Å × 82 Å × 30 Å, and then the misorientation was generated by rotating the left and right crystals by $-\theta/2$ and $+\theta/2$, respectively, around the z axis ([001]; periodicity was retained in the [001] direction). Finally, the atoms on the left and right crystals were carefully deleted along the x axis ([100]) and y axis ([010]) directions to form an interface and periodicity in those directions, respectively (the final dimensions of each crystal were 30 Å × 30 Å × 30 Å). After construction of the model, the structure was minimized using a steepest-descent method and then relaxed at 300 K and 1 atm in NPT (amount of substance (N), pressure (P) and temperature (T); ensemble for 1 ns, with 1 fs time steps (Supplementary Fig. 8). Then, to maintain periodicity in all directions, a vacuum was added in the x direction between periodic images by expanding the box size to 60 Å. The structure was then equilibrated at 300 K and 1 atm for 500 ps in a NPT ensemble (pressure s only controlled in the y and z directions), and then equilibrated at 300 K for another 500 ps in a NVT ensemble (V, volume). After preparation and equilibration of the bicrystal, a steer MD method with a high stiffness of 500 kcal mol^{-1} Å^{-2} and with a constant velocity of 0.025 Å ps^{-1} was used to apply tensile loading to the free boundary atoms of the right crystal (atoms within 5 Å distance from rightmost atoms), while keeping the free boundary atoms of the left crystal (atoms within 5 Å distance from leftmost atoms) fixed. During the steer MD simulation, the positions of the Ca and P atoms at the boundaries in the x direction were kept fixed and stress and strain values were recorded to obtain the strength (maximum stress) and toughness (approximately the area below the stress–strain curve) for each misorientation (as shown in Fig. 6f). Three different initial configurations (saved snapshots with 200-ps intervals after equilibrium) were tested to add statistical variations.

To calculate the amorphization work in HAP during a high-speed impact, non-equilibrium MD simulations of shock conditions were performed using a piston moving along the z axis [001] with constant velocity. The HAP crystal structure and force field used for shock simulations are the same as those mentioned above. To have a large sample for shock propagation, the unit cell was replicated by $3\times2\times20$ to the final approximate dimensions of $30\,\text{Å}\times30\,\text{Å}\times200\,\text{Å}$. As the periodicity cannot be applied in the shock direction, the dimension of the sample in the shock direction is much larger. The sample was then minimized using the steepest-descent method and then equilibrated at 300 K in the NVT ensemble for 500 ps with 0.5-fs time steps with the periodic boundary conditions only applied in the [100] and [010] directions (transverse to the shock propagation). The equilibrated structure checked by observing the variation of root-mean-square deviation during the simulation. The piston was then moved along the [001] direction with a velocity up to $5\,\text{km s}^{-1}$ associated with 100 GPa pressure. For the amorphization of HAP under shock compression and following a recent work for the amorphization of silicon carbide[60], the Patel–Cohen formulation for the effect of pressure and shear stress on amorphization work was employed:

$$W = P\epsilon + \tau\gamma \tag{2}$$

where W is the amorphization work, P the hydrostatic pressure, ϵ the longitudinal strain in the shock direction, τ the shear stress and γ the shear strain. The simulation results for W and the τ/P ratio at different longitudinal pressure and snapshots of the initial and final structures after shock propagation are shown in Supplementary Fig. 8. For the impact stress of ~0.98 GPa in the current impact tests, the amorphization work and τ/P were about $\sim0.038\,\text{GJ m}^{-3}$ and 1.4, respectively.

To understanding the strain-rate effect on the bicontinuous composite of the HAP nanoparticle and organic phase, a coarse-grained molecular dynamic model was used to represent the mechanical behaviour of HAP and the organic phase in a simple cubic bicontinuous structure (as shown in Fig. 5b with blue and red colours, respectively). The interaction of coarse-grained beads in HAP and the organic phase is defined through the Morse potential:

$$E = D_0\left[e^{-2\alpha(r-r_0)} - 2e^{-\alpha(r-r_0)}\right] \tag{3}$$

where E is the pairwise potential, D_0 the potential depth, r the distance between pairs, r_0 the equilibrium distance between pairs and α a parameter that controls the width of the potential (the hardness and/or softness of the interaction). The coarse-grained structure is a face-centred cubic structure with a 1 nm lattice distance and total dimensions of $20\,\text{nm}\times20\,\text{nm}\times20\,\text{nm}$ (Fig. 6b). For each bead, the masses of $450\,\text{g mol}^{-1}$ and $150\,\text{g mol}^{-1}$ were selected to represent the density of $3.2\,\text{g cm}^{-3}$ and $1.1\,\text{g cm}^{-3}$ for HAP and the organic phase, respectively. The values of D_0, r_0 and α were selected in such a way as to produce the mechanical properties of HAP as in the Morse potential; the failure strain, maximum force and stiffness were defined by $\varepsilon_f=\ln2/(\alpha r_0)$, $F_{max}=\alpha D_0/2$ and $K=2\alpha^2D_0$, respectively. For the soft phase, the strength and stiffness were assumed to be one order of magnitude smaller and the failure strain was assumed to be 50% higher than that of HAP. For the interaction of the soft phase with HAP, Lorentz–Berthelot mixing rule for D_0, and α was used. After construction of the model, the system was equilibrated at 300 K for 500 ps in the NVT ensemble and then equilibrated at 300 K and 1.0 atm for 2 ns in the NPT ensemble. The compressive strain with various strain rates (from 1 to $1\times10^{-4}\,\text{ps}^{-1}$) was then applied to the system in one direction by changing the box size, with the pressure kept fixed at 1.0 atm in the other two directions. It is worth mentioning that the values of the strain rates at molecular scales were typically higher than those at the macroscale[61–63]. For example, in a study on the high-strain-rate tensile testing of silver nanowires, the strain-rate values for experiments and MD simulations were in the range from $0.0002\,\text{s}^{-1}$ to $2\,\text{s}^{-1}$ and from 10^6 to $10^8\,\text{s}^{-1}$, respectively[61]. The stress–strain curves for different strain rates and the deformed structures of HAP nanoparticles at high and low strain rates are shown in Fig. 6e.

Reporting Summary. Further information on research design is available in the Nature Research Reporting Summary linked to this article.

Data availability

All the data that support the findings of this study are provided in the Supplementary Information and source data. Source data are provided with this paper.

References

51. Labuda, A., Kocuń, M., Meinhold, W., Walters, D. & Proksch, R. Generalized hertz model for bimodal nanomechanical mapping. *Beilstein J. Nanotechnol.* **7**, 970–982 (2016).
52. Kocun, M., Labuda, A., Meinhold, W., Revenko, I. N. & Proksch, R. Fast, high resolution, and wide modulus range nanomechanical mapping with bimodal tapping mode. *ACS Nano* **11**, 10097–10105 (2017).
53. Benaglia, S., Amo, C. A. & Garcia, R. Fast, quantitative and high resolution mapping of viscoelastic properties with bimodal AFM. *Nanoscale* **11**, 15289–15297 (2019).
54. Asif, S. S., Wahl, K. & Colton, R. Nanoindentation and contact stiffness measurement using force modulation with a capacitive load-displacement transducer. *Rev. Sci. Instrum.* **70**, 2408–2413 (1999).
55. Syed Asif, S., Wahl, K., Colton, R. & Warren, O. Quantitative imaging of nanoscale mechanical properties using hybrid nanoindentation and force modulation. *J. Appl. Phys.* **90**, 1192–1200 (2001).
56. Plimpton, S. Fast parallel algorithms for short-range molecular dynamics. *J. Comput. Phys.* **117**, 1–19 (1995).
57. Lin, T.-J. & Heinz, H. Accurate force field parameters and pH resolved surface models for hydroxyapatite to understand structure, mechanics, hydration, and biological interfaces. *J. Phys. Chem. C* **120**, 4975–4992 (2016).
58. Ching, W., Rulis, P. & Misra, A. Ab initio elastic properties and tensile strength of crystalline hydroxyapatite. *Acta Biomater.* **5**, 3067–3075 (2009).
59. Espanol, M., Portillo, J., Manero, J.-M. & Ginebra, M.-P. Investigation of the hydroxyapatite obtained as hydrolysis product of α-tricalcium phosphate by transmission electron microscopy. *CrystEngComm* **12**, 3318–3326 (2010).
60. Zhao, S. et al. Shock-induced amorphization in silicon carbide. *Acta Mater.* **158**, 206–213 (2018).
61. Lin, S., Cai, Z., Wang, Y., Zhao, L. & Zhai, C. Tailored morphology and highly enhanced phonon transport in polymer fibers: a multiscale computational framework. *npj Comput. Mater.* **5**, 126 (2019).
62. Ramachandramoorthy, R., Gao, W., Bernal, R. & Espinosa, H. High strain rate tensile testing of silver nanowires: rate-dependent brittle-to-ductile transition. *Nano Lett.* **16**, 255–263 (2016).
63. Fang, Q., Tian, Y., Wu, H. & Li, J. Revealing the deformation mechanism of amorphous polyethylene subjected to cycle loading via molecular dynamics simulations. *RSC Adv.* **8**, 32377–32386 (2018).

Acknowledgements

We acknowledge N. A. Yaraghi for his work and support in the initial stage of the project. We also acknowledge L. G. Hector for his support and discussions on the application of these designs. We acknowledge funding from the Air Force Office of Scientific Research Multi-University Research Initiative (MURI AFOSR-FA9550-15-1-0009); D.K. also acknowledges funding from the Air Force Office of Scientific Research (AFOSR-FA9550-10-1-0322, AFOSR-FA9550-17-1-0449 and AFOSR-FA9550-18-1-0424) and the Army Research Office (ARO-W911NF-16-1-0208).

Author contributions

D.K. initiated and planned the project. W.H. performed the sample preparation, characterization and mechanical experiments. M.S., N.G.-Z. and P.Z. performed the computational simulations and provided analyses and writing on simulations. N.D.K. and J.L. did the AFM tests and data analysis. L.C. performed TGA and DSC, T.W. performed the TEM sample staining and EDX, S.B. and W.H. performed the in situ TEM mechanical tests. D.S. and P.M. performed the nanoindentation and nanoDMA tests and data analysis. K.N.B. provided support on the TEM experiments as well as data analysis. R.C. provided discussion on the evolutionary and biological aspects of the manuscript. W.H. and D.K. wrote the manuscript. All the authors made edits and revisions on the final draft.

Competing interests

The authors declare no competing interests.

Additional information

Extended data is available for this paper at https://doi.org/10.1038/s41563-020-0768-7.

Supplementary information is available for this paper at https://doi.org/10.1038/s41563-020-0768-7.

Correspondence and requests for materials should be addressed to D.K.

Reprints and permissions information is available at www.nature.com/reprints.

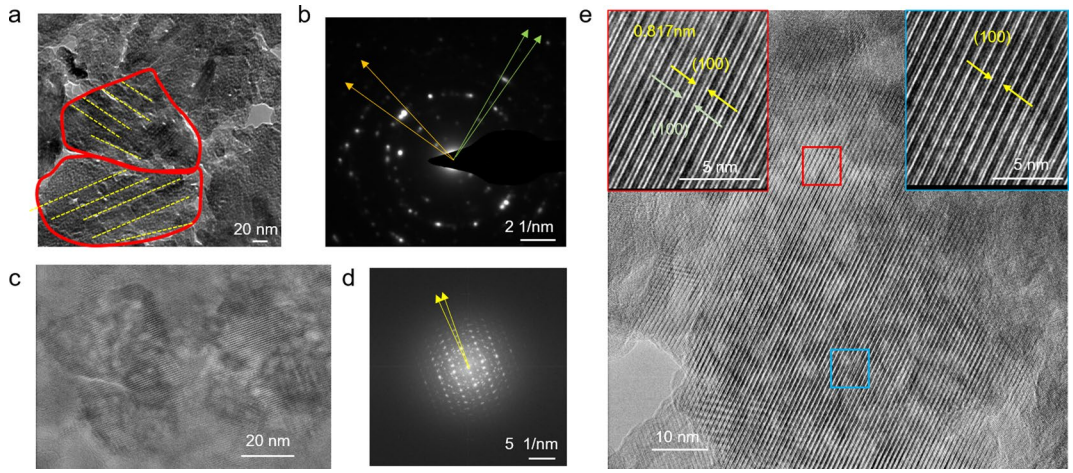

Extended Data Fig. 1 | TEM and HRTEM micrographs of hydroxyapatite (HAP) composite nanoparticles within the impact surface. TEM and HRTEM micrographs of hydroxyapatite (HAP) composite nanoparticles within the impact surface. **a**, Secondary HAP nanoparticles marked with red outlines. The yellow dashed lines show the alignment of primary particles within a single secondary HAP particle. **b**, SAED pattern from the TEM image in (**a**). The small arcs indicate slight mis-alignments of nanocrystals within the secondary particle. **c**, HRTEM image of a single HAP particle, with brighter contrast regions suggesting the presence of a secondary phase. **d**, FFT of the particle in (**c**). (**e**) HRTEM of the (100) lattice in the HAP nanocrystals. Insets: Stacking faults are observed within primary particles. Three independent dactyl clubs from 3 different mantis shrimps were examined in TEM. Similar results as shown in (**a**–**e**) were observed.

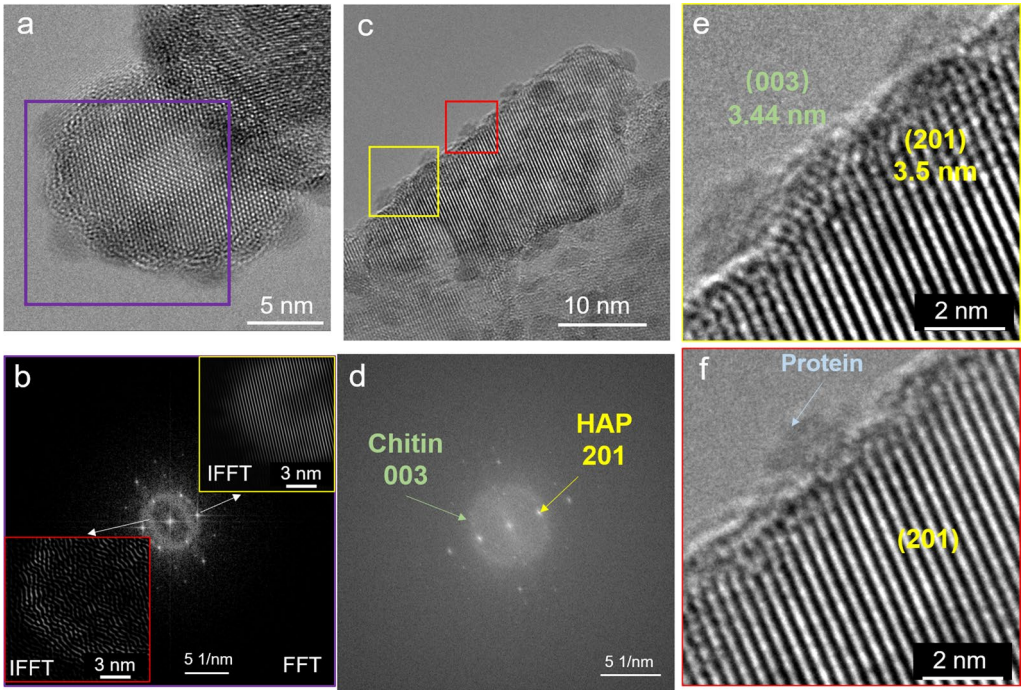

Extended Data Fig. 2 | HRTEM of uranyl acetate and lead citrate stained HAP nanoparticles on the impact surface. HRTEM of uranyl acetate and lead citrate stained HAP nanoparticles on the impact surface. The reduced ordering in protein complexes provide a higher permeability for the heavy metal staining solution, resulting in greater contrast in the TEM micrograph. **a**, HRTEM of a HAP nanoparticle, showing chitin macromolecules wrapping around the HAP crystal. **b**, FFT of the HAP crystal lattice indicated with a purple box in (**a**). Both diffraction spots and rings are observed in the FFT pattern. Inverse Fast Fourier Transform (IFFT) is performed on the diffraction spots and rings, separately. The yellow box (upper, right inset) shows the HAP lattice after IFFT, while red box (lower, left) shows the location of chitin macromolecules. **c**, HRTEM of a HAP nanoparticle. **d**, FFT of the HAP nanoparticle in (**c**). The (201) reflection from HAP is indicated with a yellow arrow, whereas the (003) planes of chitin (diffraction ring) are highlighted by the green arrow. **e**, **f**, HRTEM showing the interface between chitin macromolecules and a HAP nanocrystal. The (201) crystal planes of HAP appear adjacent with (003) planes of chitin, suggesting a potential epitaxial growth of HAP on chitin macromolecules. Three independent dactyl clubs from 3 different mantis shrimps were examined in HRTEM. Similar results as shown in (**a**–**f**) were observed.

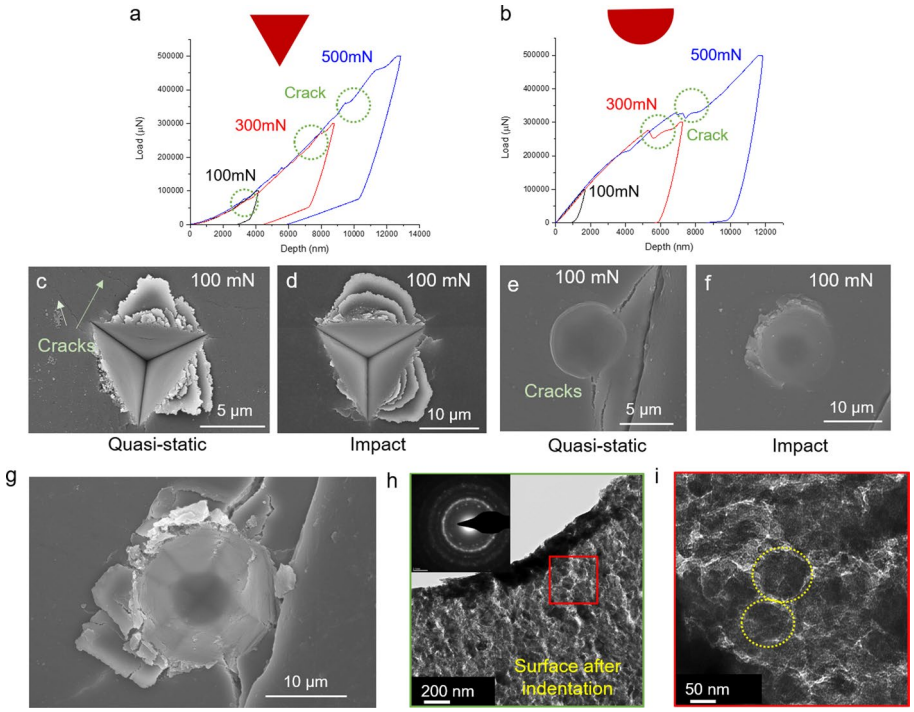

Extended Data Fig. 3 | Strain-rate-dependent behaviour in the impact surface of dactyl club. Strain-rate-dependent behaviour in the impact surface of dactyl club. Load–displacement curves of quasi-static nanoindentation on the impact surface with a sharp cube corner **a**, and a blunt spherical indenter head **b**, **c**–**f**, SEM micrographs of the damage modes in quasi-static nanoindentation and impacts with sharp and blunt indenter heads. **g**, SEM images showing particle pile up and crack initiation and propagation. **h**, **i**, TEM images of HAP nanoparticles after indentation. The secondary HAP particles remain intact after quasi-static nanoindentation. Quasi-static indentation tests on five independent locations within two different dactyl clubs were performed and examined. Similar damage modes shown in (**c**–**i**) were observed.

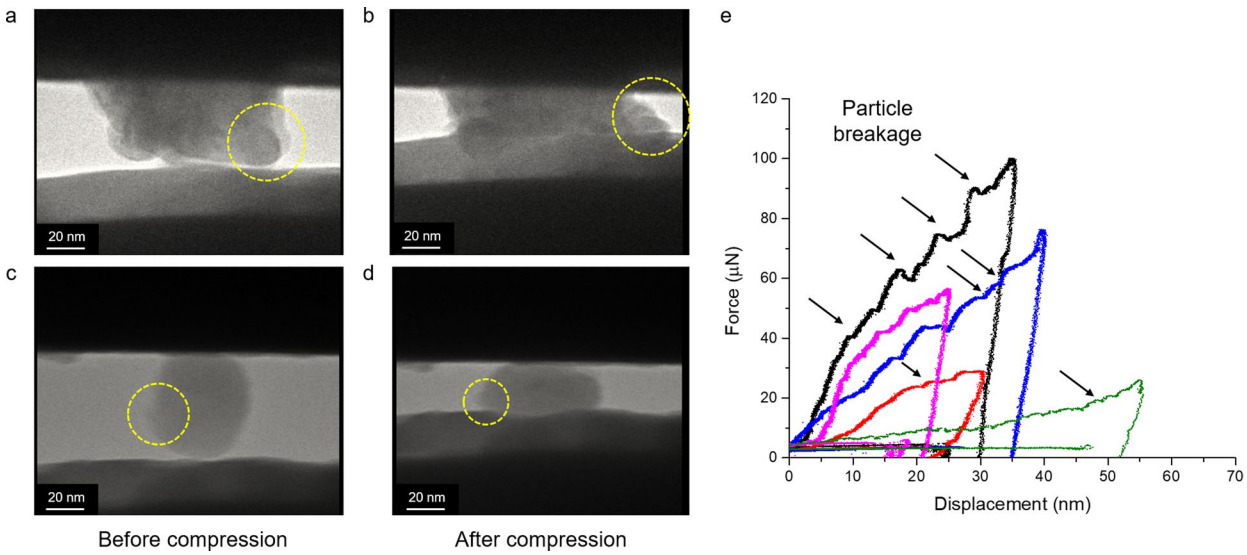

Extended Data Fig. 4 | In situ compression tests of single HAP nanoparticles. In situ compression tests of single HAP nanoparticles. **a**–**d**, HAP nanoparticle before and after compression tests, indicating particle breakage. Five different nanoparticles were tested. Similar particle breakage was noticed. **e**, Load versus displacement curves of different tests. The breakage of particles and energy dissipation events are marked with back arrows. The total energy dissipation during compression is calculated from the integration of the force-displacement curves.

nature research

Corresponding author(s): David Kisailus

Last updated by author(s): Jun 27, 2020

Reporting Summary

Nature Research wishes to improve the reproducibility of the work that we publish. This form provides structure for consistency and transparency in reporting. For further information on Nature Research policies, see Authors & Referees and the Editorial Policy Checklist.

Statistics

For all statistical analyses, confirm that the following items are present in the figure legend, table legend, main text, or Methods section.

n/a	Confirmed
☐	☒ The exact sample size (*n*) for each experimental group/condition, given as a discrete number and unit of measurement
☐	☒ A statement on whether measurements were taken from distinct samples or whether the same sample was measured repeatedly
☒	☐ The statistical test(s) used AND whether they are one- or two-sided *Only common tests should be described solely by name; describe more complex techniques in the Methods section.*
☒	☐ A description of all covariates tested
☐	☒ A description of any assumptions or corrections, such as tests of normality and adjustment for multiple comparisons
☐	☒ A full description of the statistical parameters including central tendency (e.g. means) or other basic estimates (e.g. regression coefficient) AND variation (e.g. standard deviation) or associated estimates of uncertainty (e.g. confidence intervals)
☒	☐ For null hypothesis testing, the test statistic (e.g. *F*, *t*, *r*) with confidence intervals, effect sizes, degrees of freedom and *P* value noted *Give P values as exact values whenever suitable.*
☒	☐ For Bayesian analysis, information on the choice of priors and Markov chain Monte Carlo settings
☒	☐ For hierarchical and complex designs, identification of the appropriate level for tests and full reporting of outcomes
☒	☐ Estimates of effect sizes (e.g. Cohen's *d*, Pearson's *r*), indicating how they were calculated

Our web collection on statistics for biologists contains articles on many of the points above.

Software and code

Policy information about availability of computer code

Data collection	TEM Imaging & Analysis (TIA) associated with TEM version 4.0
Data analysis	Solidworks 2019, TEM Imaging & Analysis (TIA) associated with TEM 4.0, Origin 9.0, VESTA 3.4.5, GetReal Software 16, LAMMPS (5 June 2019)

For manuscripts utilizing custom algorithms or software that are central to the research but not yet described in published literature, software must be made available to editors/reviewers. We strongly encourage code deposition in a community repository (e.g. GitHub). See the Nature Research guidelines for submitting code & software for further information.

Data

Policy information about availability of data

All manuscripts must include a data availability statement. This statement should provide the following information, where applicable:

- Accession codes, unique identifiers, or web links for publicly available datasets
- A list of figures that have associated raw data
- A description of any restrictions on data availability

The data that support the findings of this study are available from the authors on reasonable request, see author contributions for specific data sets.

Field-specific reporting

Please select the one below that is the best fit for your research. If you are not sure, read the appropriate sections before making your selection.

☒ Life sciences ☐ Behavioural & social sciences ☐ Ecological, evolutionary & environmental sciences

Life sciences study design

All studies must disclose on these points even when the disclosure is negative.

Sample size	No sample-size calculation is needed in this study. Mantis shrimp dactyl clubs were acquired from at least three different adult individuals growing at different time, which are sufficient to investigate their structure and materials properties. There is no big differences of structures and material properties among different individuals.
Data exclusions	No data was excluded from the analyses.
Replication	All the structures and mechanical properties tested in different samples from different individuals are similar and reproducible. We have been testing samples from at least three individuals to make sure the reproducibility of the experimental findings.
Randomization	This is not relevant to our study, since we don't have different experimental groups.
Blinding	Blinding is not relevant to this study, since we don't have different experimental groups here.

Reporting for specific materials, systems and methods

We require information from authors about some types of materials, experimental systems and methods used in many studies. Here, indicate whether each material, system or method listed is relevant to your study. If you are not sure if a list item applies to your research, read the appropriate section before selecting a response.

Materials & experimental systems

n/a	Involved in the study
☒	☐ Antibodies
☒	☐ Eukaryotic cell lines
☒	☐ Palaeontology
☐	☒ Animals and other organisms
☒	☐ Human research participants
☒	☐ Clinical data

Methods

n/a	Involved in the study
☒	☐ ChIP-seq
☒	☐ Flow cytometry
☒	☐ MRI-based neuroimaging

Animals and other organisms

Policy information about studies involving animals; ARRIVE guidelines recommended for reporting animal research

Laboratory animals	The study did not involve laboratory animals.
Wild animals	The mantis shrimps studied in this research were purchased from a commercial source, the Tropical Reef Store in California, USA. The species of the mantis shrimp is Odontodactylus scyllarus. The mantis shrimps were caught in the Pacific Ocean by the store. The live mantis shrimps are transported in a seawater container and via flight. The mantis shrimps were kept alive before further studies. When extracting dactyl club samples, live mantis shrimps were first immersed in eugenol solution for anesthesia purpose. Mantis shrimps are still alive after extracting of dactyl clubs. However, they will died naturally after couple of months.
Field-collected samples	The study did not involve samples collected from field.
Ethics oversight	No ethical approval or guidance required for this study.

Note that full information on the approval of the study protocol must also be provided in the manuscript.